AIAA JOURNAL
Vol. 31, No. 2, February 1993

Computation of Unsteady Shock-Induced Combustion Using Logarithmic Species Conservation Equations

Gregory J. Wilson*
Eloret Institute, Palo Alto, California 94303
and
Myles A. Sussman†
Stanford University, Stanford, California 94305

Numerical simulations are used to investigate periodic combustion instabilities observed in ballistic-range experiments of blunt bodies flying at supersonic speeds through hydrogen-air mixtures. The computations are validated by comparing experimental shadowgraphs with shadowgraphs created from the computed flowfields and by comparing the experimentally measured instability frequencies with computed frequencies. The numerical simulations use a logarithmic transformation of the species conservation equations as a way to reduce the grid requirements for computing shock-induced combustion. The transformation is applied to the Euler equations coupled to a detailed hydrogen-air chemical reaction mechanism with 13 species and 33 reactions. The resulting differential equations are solved using a finite volume formulation and a two-step predictor-corrector scheme to advance the solution in time. Results are presented and compared for both a flux-vector splitting scheme and an upwind TVD scheme. The computations add insight to the physical processes observed in the experiments and the numerical methods needed to simulate them. The usefulness of the ballistic-range experiments for the validation of numerical techniques and chemical kinetic models is also demonstrated.

Introduction

BALLISTIC-RANGE experiments performed in the 1960s and early 1970s[1-7] provide excellent data for studying the coupling between supersonic fluid dynamics and nonequilibrium chemical kinetics as well as for evaluating combustion flow codes. In these experiments, small projectiles were fired at supersonic speeds into a variety of premixed combustible mixtures. Shadowgraphs of the flowfields exhibit two distinguishing features: one is the bow shock ahead of the projectile and the other is an energy-release front created by the ignition of the heated mixture behind the bow shock. Both features can be seen in Fig. 1 in the shadowgraph by Lehr[5] of a steady ballistic-range experiment at Mach 6.46. The region between the bow shock and the energy-release front is called the induction zone, and it exists because there is an ignition delay caused by chemical nonequilibrium. The induction zone is characterized by near-constant values (the postshock values) of temperature, density, pressure, and velocity. The size of the induction zone is determined by the fluid speed downstream of the shock and the ignition time corresponding to the postshock conditions. When ignition occurs, the energy is released over an interval much shorter than the ignition delay time and appears as a discontinuity that is referred to as the energy-release front. Across the energy-release front the pressure is nearly constant, the temperature rises, and the density drops. This can be seen in the shadowgraph where the shift from light to dark across the bow shock corresponds to the density increase across the shock whereas the shift from dark to light across the energy-release front indicates a drop in density.

Depending on the conditions of the experiment, one will observe either steady or unsteady flow. Projectile speeds greater than the detonation wave speed tend to induce steady flows whereas speeds less than the detonation wave speed can produce unsteady flows. The unsteady flows are characterized by two different regimes. One is called the regular regime, and the other is called the large disturbance or irregular regime. All of the unsteady simulations presented in this work are in the regular regime (see Alpert and Toong[7] for more on the large disturbance regime). Figures 2a and 2b show an unsteady ballistic-range experiment with the same freestream conditions as in Fig. 1 except that the projectile speed is Mach 4.79. The shadowgraphs reveal remarkable high-frequency oscillations. The frequency of the instability is approximately 720 kHz as deduced from the projectile speed and counting the number of oscillations that occur over a known distance. Figures 2a and 2b are from the same ballistic-range shot but show different view angles. The view axis of Fig. 2a is perpendicular to the

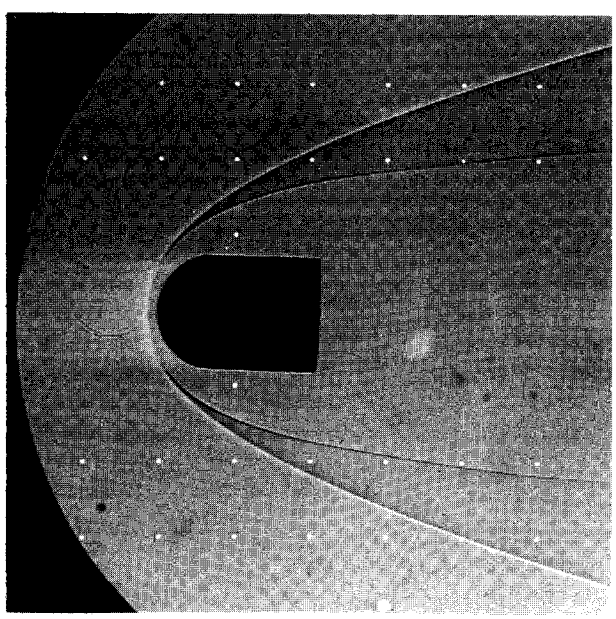

Fig. 1 Shadowgraph of a spherical nose projectile moving at Mach 6.46 in a stoichiometric hydrogen-air mixture (courtesy of H. F. Lehr).

Received Dec. 19, 1991; revision received July 20, 1992; accepted for publication July 24, 1992.

*Research Scientist; mailing address, NASA Ames Research Center, MS 230-2, Moffett Field, CA 94305. Member AIAA.

†Graduate Student, Department of Aeronautics and Astronautics. Student Member AIAA.

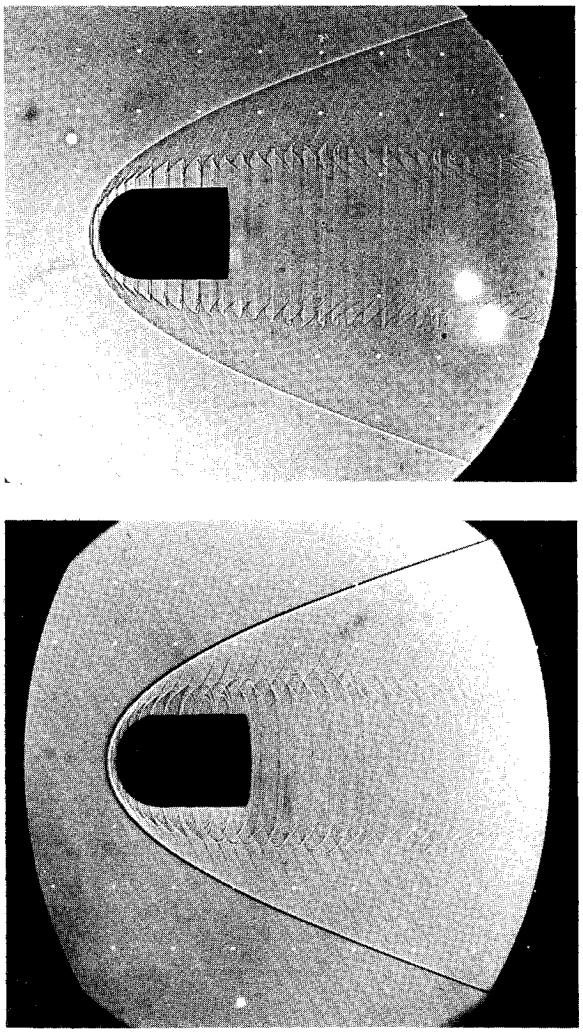

Fig. 2 Shadowgraph of a spherical nose projectile moving at Mach 4.79 in a stoichiometric hydrogen-air mixture: a) side view, b) off-axis view (courtesy of H. F. Lehr).

flight axis, and Fig. 2b is off axis and reveals some of the three-dimensional structure of the flowfield. Although complex in many ways, the physics of these ballistic-range flows are predominantly driven by reaction kinetics and convection phenomena; therefore, the complications and uncertainties of diffusion and mixing are removed from the problem. As a result, differences between the experimental data and numerical simulations can be attributed either to numerical errors or to improperly modeled chemical kinetics.

An earlier work by Wilson and MacCormack[8] focused on the steady ballistic-range experiments and demonstrated the physical and numerical modeling requirements for accurate computations of these flows. It was shown that a primary requirement is adequate resolution in the induction zone between the bow shock and the energy-release front. Fine grid resolution is needed because the mass fractions of the important radical species change exponentially in this region. Adaptive grid techniques offer one way to efficiently distribute points; however, such techniques are not always adequate. The induction zone may cover such a large region of the flowfield that grid requirements still remain large. Furthermore, the small grid spacings in the adapted regions may result in undesired time step limitations. Additional difficulty is added by the presence of the complex flow structures seen in the unsteady ballistic-range cases because there is no primary direction for adapting.

As an alternative to adapting the grid, the simulations presented in this paper use the logarithmic transformation of the species conservation equations presented by Sussman and Wilson.[9] Other researchers have realized the potential advantages of such an approach because the exponential growth of the radical mass fractions that occurs in the induction zone can be accurately represented with fewer points if a logarithmic transformation is used. The formulation of Sussman and Wilson is unique because it can be implemented in modern shock-capturing computational fluid dynamics (CFD) schemes.

The use of the logarithmic transformation allows accurate simulations of both steady and unsteady ballistic-range experiments on grids more coarse than have been used in prior works.[8,10] The reduction in grid size, and thus computational resources, permits the use of a detailed chemical model, which enables direct comparisons of the simulations to the experiments to be made for the first time. In particular, measured oscillation frequencies are compared with those predicted by the computations.

The simulations in this work add insight into the combustion instabilities observed in ballistic-range experiments and allow previously proposed mechanisms for the instabilities to be assessed. In particular, this work considers the wave interaction mechanism of McVey and Toong[6] and the modified mechanism proposed by Matsuo and Fujiwara.[10] McVey and Toong developed their mechanism by using experimental data and analytical calculations. Matsuo and Fujiwara used modern computational fluid dynamics techniques, fine grids, and a two-equation, two-step combustion model to do qualitative simulations that led them to propose their modified mechanism. In addition to adding greater physical understanding, the current method also provides a tool to validate and possibly "tune" proposed chemical kinetic models.

The chemical kinetic model used in this paper can be found in Wilson and MacCormack.[8] It is the mechanism proposed by Jachimowski[11] containing 13 chemical species and 33 reactions except that one of the reaction rate expressions (the expression most influential for ignition times) has been replaced by an expression recommended by another source. This modification was found by Wilson and MacCormack[8] to give better agreement with experiment. Additional details on the chemical kinetics are found in Wilson.[12]

Logarithmic Form of the Species Conservation Equation

This section gives an overview of the logarithmic transformation of the species conservation equations as presented by Sussman and Wilson.[9] The transformation is based on the definition

$$\pi_s \equiv \rho \ell n\left(\frac{\rho_s}{\rho}\right) \equiv \rho \ell n(c_s) \tag{1}$$

where ρ is the total density, ρ_s is the density of species s, and c_s is the mass fraction of species s. A special property of the relationship in Eq. (1) is that it can be used along with the total mass conservation equation,

$$\frac{\partial}{\partial t}\rho + \frac{\partial}{\partial x_j}\rho u_j = 0 \tag{2}$$

to transform the species mass conservation equation (neglecting diffusion),

$$\frac{\partial}{\partial t}\rho_s + \frac{\partial}{\partial x_j}\rho_s u_j = w_s \tag{3}$$

into a transformed species equation,

$$\frac{\partial}{\partial t}\pi_s + \frac{\partial}{\partial x_j}\pi_s u_j = w_s \frac{\rho}{\rho_s} \tag{4}$$

where u_j is the jth component of velocity, and w_s is the chemical source term for species s. The transformation from Eq. (2) to Eq. (4) retains conservation form.

In theory, all of the species mass conservation equations can be replaced with a corresponding transformed species equation in the form of Eq. (4). In practice, however, this is not done. Although Eq. (4) is in conservation form, its use does not guarantee conservation of mass or conservation of the individual elements. Enforcement of these constraints is achieved by including element mass conservation equations in the form

$$\frac{\partial}{\partial t}\rho_e^* + \frac{\partial}{\partial x_j}\rho_e^* u_j = 0 \tag{5}$$

where ρ_e^* is the total density of element e contained in all of the species (the * is used to avoid confusion between element and species densities; $\rho_N^* \neq \rho_N$). There are as many of these equations as there are elements in the chemical model. The total density is given by

$$\rho = \sum_{e=1}^{N\text{elements}} \rho_e^* \tag{6}$$

The chemical reaction mechanism used in this work involves 13 species: N_2, O_2, H_2, NO, OH, NO_2, HNO, HO_2, H_2O, H_2O_2, N, O, and H. Since three elements are present in the mechanism (N, O, and H), three equations of the form of Eq. (5) are required. The densities ρ_N^*, ρ_O^*, and ρ_H^* are defined using expressions that are the sum of the contributions from each of the species containing the element of interest. For example, the expression for ρ_N^* depends on the densities of N_2, NO, NO_2, HNO, and N and is written

$$\frac{\rho_N^*}{M_N} = 2\frac{\rho_{N_2}}{M_{N_2}} + \frac{\rho_{NO}}{M_{NO}} + \frac{\rho_{NO_2}}{M_{NO_2}} + \frac{\rho_{HNO}}{M_{HNO}} + \frac{\rho_N}{M_N} \tag{7}$$

where M_s is the molecular mass of species s. The choice of which three species conservation equations to replace with element mass conservation equations is not unique. The selection of N_2, O_2, and H_2 seems appropriate because these species do not exhibit exponential mass fraction growth. The remaining 10 species conservation equations (for species NO, OH, NO_2, HNO, HO_2, H_2O, H_2O_2, N, O, and H) are written in the form of Eq. (4). The densities of N_2, O_2, and H_2 are computed from relations of the type of Eq. (7).

Numerical Formulation

This section presents the Euler equations with the logarithmic form of the species conservation equations. The 13 species mass conservation equations of the conventional formulation have been replaced by equations of similar form except that 3 are elemental mass conservation equations [see Eq. (5)] and 10 are in the logarithmic variable π_s [see Eq. (4)]. The momentum and energy equations in the logarithmic formulation are the same as they were in the conventional formulation. In vector notation the governing equations are written

$$\frac{\partial U}{\partial t} + \frac{\partial F}{\partial x} + \frac{\partial G}{\partial y} = W \tag{8}$$

where U is the state vector, F and G are the convective (inviscid) flux vectors in the x and y coordinate directions, respectively, and W is the vector of source terms. These vectors are given next:

$$U = \begin{bmatrix} \rho_N^* \\ \rho_O^* \\ \rho_H^* \\ \pi_{NO} \\ \vdots \\ \pi_H \\ \rho u \\ \rho v \\ E_v \\ E \end{bmatrix}, \quad F = \begin{bmatrix} \rho_N^* u \\ \rho_O^* u \\ \rho_H^* u \\ \pi_{NO} u \\ \vdots \\ \pi_H u \\ \rho u^2 + p \\ \rho uv \\ uE_v \\ u(E+p) \end{bmatrix}$$

$$G = \begin{bmatrix} \rho_N^* v \\ \rho_O^* v \\ \rho_H^* v \\ \pi_{NO} v \\ \vdots \\ \pi_H v \\ \rho uv \\ \rho v^2 + p \\ vE_v \\ v(E+p) \end{bmatrix}, \quad W = \begin{bmatrix} 0 \\ 0 \\ 0 \\ w_{NO}/c_{NO} \\ \vdots \\ w_H/c_H \\ 0 \\ 0 \\ w_v \\ 0 \end{bmatrix} \tag{9}$$

where E_v is vibrational energy per unit volume, w_v is the source term representing vibrational relaxation, E is the total energy per unit volume, and p is pressure. A separate vibrational energy equation is not required for the present computations but has been retained from previous work. For the cases presented here, thermal equilibrium is simulated by using a small time constant for vibrational relaxation.

In Eq. (8), pressure is a homogeneous function of degree one in the conserved variables U and the flux Jacobians ($\partial F/\partial U$ and $\partial G/\partial U$) have the same eigenvalues as that of the formulation with the conventional form of the species mass conservation equations. Therefore, existing numerical techniques can be applied in a straightforward manner. In this work, two commonly used shock-capturing numerical techniques are employed. One is a modified Steger-Warming flux-vector splitting technique based on work by MacCormack[13] and Candler[14] (this method shall be referred to as the flux-vector splitting scheme) and the other is the Harten-Yee upwind total variation diminishing (TVD) (non-MUSCL) scheme[15] (referred to as the upwind TVD scheme). Both techniques are spatially second order and solved in a point-implicit manner. That is, the convective terms are treated explicitly whereas the source terms are treated implicitly in time (because of the small time scales of the combustion chemistry and vibrational relaxation). Therefore, a block inversion is required at each point at each time step. Details about the flux-vector splitting scheme using the logarithmic formulation can be found in Wilson.[12]

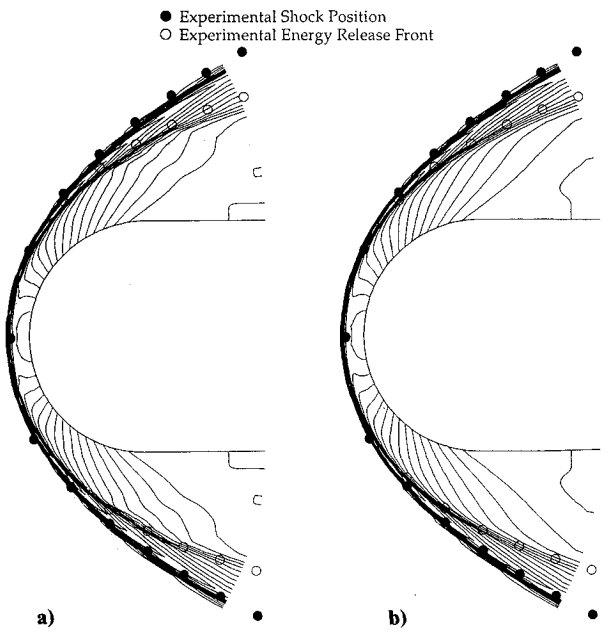

Fig. 3 Density contours from a numerical simulation of the Mach 6.46 experiment in Fig. 1: a) flux-vector splitting, b) upwind TVD.

Several practical details of the logarithmic formulation are addressed next. Because zero mass fractions are not allowed in the transformed equations, the mass fractions of the radical species must be set to small arbitrary values in the freestream (10^{-10} for this work). One-dimensional calculations show that the solutions are relatively insensitive to the freestream radical mass fractions, as long as they remain sufficiently small. An advantage of using logarithms is that mass fractions remain positive. Limiters are required to prevent the mass fractions of species not represented by a logarithm from becoming negative (N_2, O_2, and H_2). In practice, the logarithmic formulation is no less robust than the conventional formulation for the flows presented here. The cost per time step is increased by 10–20% over the conventional formulation due to the cost of computing logarithms and exponentials and also due to the increased complexity of the Jacobian of the chemical source terms.

The logarithmic formulation has limitations at interfaces (contact discontinuities) separating gases of different chemical composition. The inherent numerical diffusion for each species across such an interface is modified by the logarithmic transformation in such a way that the interface is distorted. The use of the transformation is advantageous in this work because the effect of this distortion is small. In simulations of other flows (e.g., the interface in a shock tube), such distortions may not be tolerable, and the use of the logarithmic transformation may not be warranted.

Numerical Simulations

This section presents numerical simulations of ballistic-range shadowgraphs from experiments by Lehr.[4,5] The particular experiments of interest used spherical-nosed projectiles with cylindrical afterbodies of 15-mm diameter. The cases include a range of Mach numbers so that both steady and unsteady flows are represented. All of the cases to be considered have freestream with a temperature of 292 K, a pressure of 320 mm Hg, and a premixed stoichiometric hydrogen-air mixture. At these conditions, the detonation wave speed was reported by Lehr to be Mach 5.11.

Before the unsteady cases are considered, a simulation of the steady Mach 6.46 case in Fig. 1 is shown to demonstrate the advantage of the logarithmic formulation and to give an understanding of why it is practical to use this formulation for the unsteady cases. Figure 3 contains density contours for computations of the Mach 6.46 case using flux-vector splitting and the upwind TVD methods, respectively. Both computations use the 52×52 grid shown in Fig. 4. The experimental bow shock and energy-release front positions are overplotted on the density contours and show that both numerical methods provide good agreement with the experiment. A numerical simulation using the conventional form of the species conservation equations can be found in Wilson and MacCormack.[8] Good agreement with experiment was found in that work as well, but it required an adapted 321×64 mesh (321 points around the body and 64 points normal to the body). The grid for the calculation using the logarithmic formulation is more than eight times smaller because the induction zone is adequately resolved with fewer grid points.

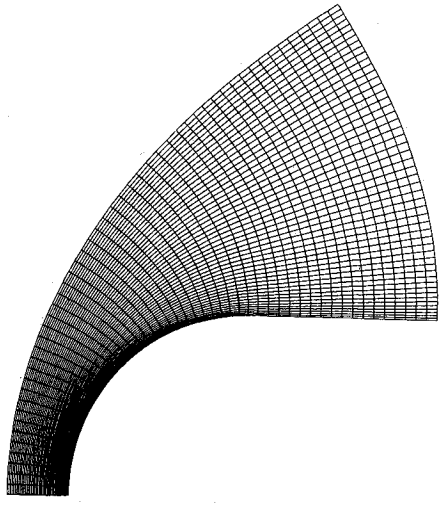

Fig. 4 52×52 grid used for the calculations presented in Fig. 3.

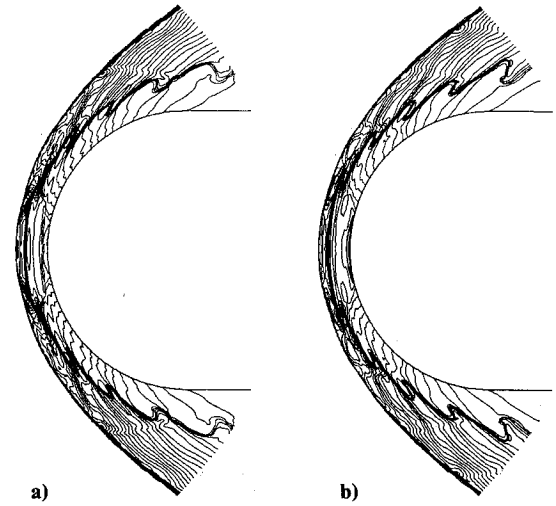

Fig. 5 Density contours from a numerical simulation of the Mach 4.79 experiment in Fig. 2: a) flux-vector splitting, b) upwind TVD.

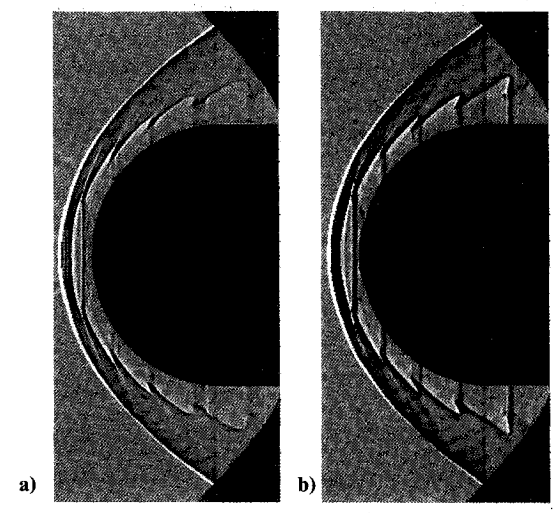

Fig. 6 Computed shadowgraphs from a numerical simulation of the Mach 4.79 experiment in Fig. 2: a) flux-vector splitting, b) upwind TVD (shadowgraphs computed by Yates[16]).

Simulations of Lehr's unsteady Mach 4.79 case shown in Fig. 2 are now presented. Density contour plots for both the flux-vector splitting and upwind TVD methods are presented in Figs. 5a and 5b, respectively. The figures represent one point in time and one point in the period of the instability (the two solutions are not at exactly corresponding points within a period) and show that both computational methods predict unsteady behavior. As in the steady computation of Fig. 3, the density contours exhibit an outer bow shock followed by an induction zone and an energy-release front. The most obvious difference between the unsteady calculation and the steady one is the pulsing structure of the energy-release front. These pulses are seen in the experimental shadowgraph with the off-axis view in Fig. 2b. The computations were started from a flowfield that was initially set to freestream conditions everywhere and advanced in time without chemistry until a bow shock was established, at which time the combustion chemistry was turned on. No other special procedures were used. The

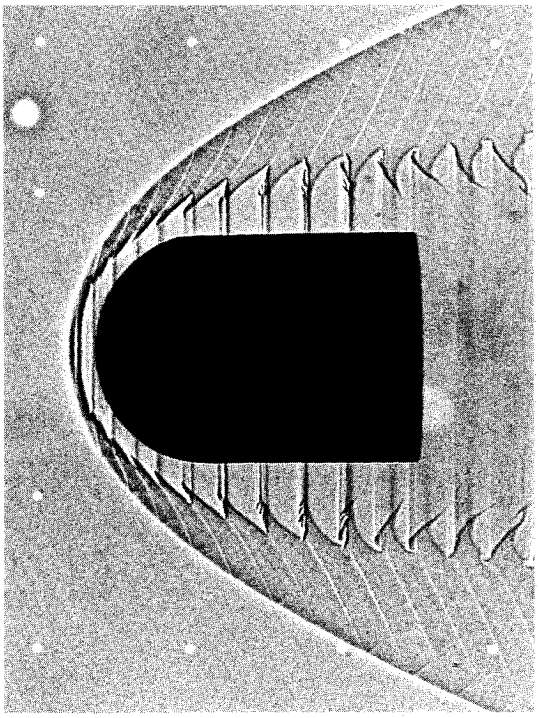

Fig. 7 Enlargement of the Mach 4.79 ballistic-range shadowgraph in Fig. 2a (courtesy of H. F. Lehr).

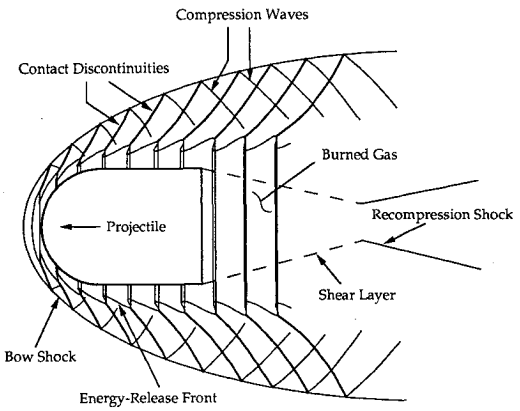

Fig. 8 Schematic diagram of the periodic flowfield structures seen in shadowgraphs of ballistic-range experiments.

computations used a nearly equally spaced 375×161 grid. Computations on a 375×81 grid yielded similar overall flow features and an oscillation frequency near that predicted by the 375×161 grid.[12] (Note that the grid required to resolve the complex unsteady flow structures negates some of the advantage that the logarithmic transformation provides. The usefulness of the transformation is the relative grid independence of the induction zone length and the instability frequency. This allows practical grid refinement studies to be done and adds confidence in the accuracy of the predicted frequencies.) The code uses approximately 2.8×10^{-4} CPU s per time step per grid point on a Cray Y-MP. Depending on the grid, the simulations required between 10,000 and 20,000 iterations and between 16 and 70 h of CPU time.

Figures 6a and 6b contain shadowgraphs computed from the flux-vector splitting and upwind TVD flowfields, respectively.[16] A comparison of these computed shadowgraphs with the enlargement of Fig. 2a presented in Fig. 7 clearly shows many similarities. Note that the pulses in the energy-release front create the vertical line pattern when the axisymmetric flowfield is projected onto a plane. There is a larger streamwise separation between the vertical lines in the computed shadowgraphs compared with the experiment, and thus the computations predict a lower frequency than the experiment. Both numerical methods predict an instability frequency of approximately 530 kHz compared with the measured value of 720 kHz. The primary difference between the flux-vector splitting and upwind TVD solutions is the resolution of the flow structures near the shoulder region of the projectile. The flux-vector splitting smears these features to a larger degree.

Further support of the computations is provided by examining the experimental and computed shadowgraphs in more detail. A schematic diagram of the flowfield that labels the different structures is found in Fig. 8. An analysis of these structures by McVey and Toong[6] identified the waves extending from each pulse of the energy-release front to the bow shock as contact discontinuities (McVey and Toong refer to them as entropy waves). Their identity was established by observing that they are convected with the local fluid speed. Compression or expansion waves would move faster than the local flow with a relative speed that depends on the speed of sound in the mixture. The waves that look like reflections of the contact discontinuities off the bow shock do move at a speed greater than the local flow and were identified as compression waves. The dark-light shadings across the waves support their asserted identities. All of these features can be observed in both the experimental and simulated shadowgraphs.

Investigation of other flowfield quantities adds information that cannot be deduced from the shadowgraphs. Pressure contours reveal that each pulse of the energy-release front creates a compression wave that travels both upstream toward the bow shock and downstream toward the projectile body. Figure 9 shows the pressure contours at one point in time. The wave patterns between the bow shock and the projectile appear quite complicated but can be understood by noting that there are primarily two families. One family is made up of compression waves originating directly from the energy-release front and the other family is made up of compression waves from the first family that have reflected off the projectile body.

Instability Mechanism

The mechanism that causes and sustains the combustion instabilities observed in the ballistic-range has not been observed experimentally. Therefore, plausible explanations for the unsteadiness have been developed by extrapolating data from outside the nose region (mostly from the shadowgraphs) and by transferring knowledge from other flow situations. It was not until the work of Toong and his associates that plausible detailed mechanisms for the regular[6] and large-disturbance[7] regimes were proposed.

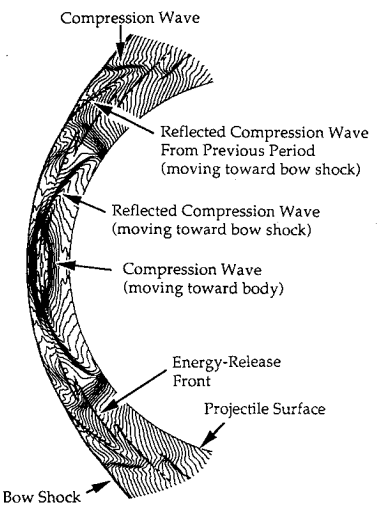

Fig. 9 Pressure contours for the Mach 4.79 case at one point in an oscillation period.

The work of McVey and Toong[6] is discussed further here because it is supported by the present numerical simulations. McVey and Toong used what they called a wave-interaction model to explain the oscillations observed in the regular regime. All of the important processes in this model occur between the energy-release front and the bow shock in the subsonic region ahead of the projectile nose. As an aid to understanding the model, several of the primary components of the model are isolated and described first.

A major component in the McVey and Toong model is the interaction between the bow shock and a compression wave. Figure 10 depicts a one-dimensional flow at several different times (time proceeds from bottom to top). Initially there is a stationary normal shock and a compression wave downstream of the shock moving toward the shock. At a later time the compression wave overtakes the shock, strengthening it and causing the shock to move forward. The strengthened shock causes a change in the fluid properties behind it. Most important for the instability is a higher fluid temperature. This higher temperature fluid is separated from the fluid that has crossed the shock at the original strength by a contact discontinuity that convects downstream. Additionally, a rarefaction wave is created that travels downstream.

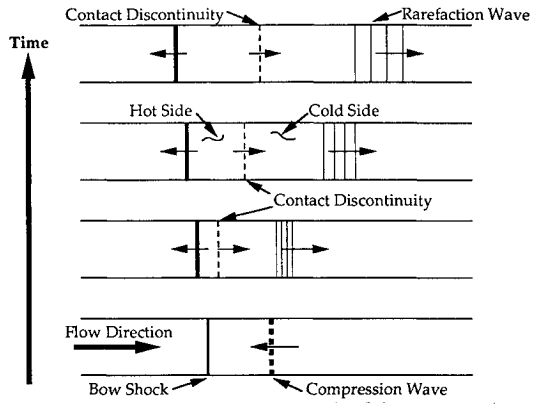

Fig. 10 Schematic diagram of a one-dimensional bow shock/compression wave interaction.

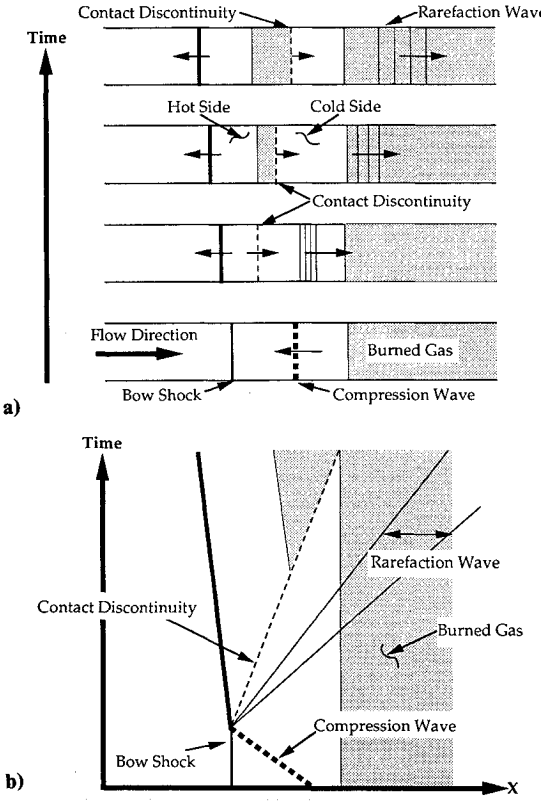

Fig. 11 Schematic diagram of a bow shock/compression wave interaction with shock-induced combustion: a) series of one-dimensional diagrams, b) *x-t* diagram.

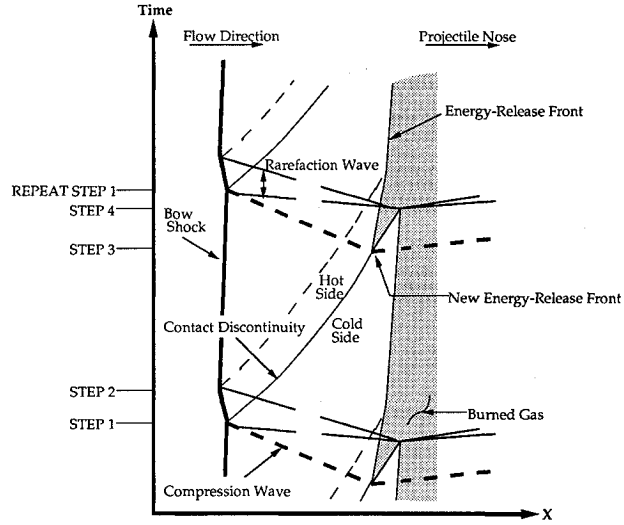

Fig. 12 McVey and Toong[6] wave interaction model.

Interesting flow features are created when the interaction of Fig. 10 is combined with the flow of a combustible mixture. This is the situation presented in Fig. 11a. As in Fig. 10, there is initially a stationary normal shock wave with a compression moving toward it from the downstream side. Now there is also burned fluid downstream of the shock at some induction length. As before, the compression wave overtakes the bow shock, strengthening it and creating a contact discontinuity and a rarefaction wave. Because the fluid on the upstream side of the contact discontinuity is hotter, it has a shorter induction time and burns more quickly. The result is that for a time there are two regions of burning, one at an induction length corresponding to the original postshock conditions, and the other at the shorter induction length corresponding to the strengthened shock. Figure 11b is an *x-t* diagram corresponding to the interaction in Fig. 11a. The general features of this diagram are recognizable in the McVey and Toong mechanism presented next.

The McVey and Toong mechanism is schematically depicted in the *x-t* diagram in Fig. 12. The diagram shows time evolution of the features along the stagnation streamline and is explained in the following four steps.

1) A compression wave on the downstream side of the bow shock overtakes the bow shock, causing the bow shock to move forward, thus creating a reflected rarefaction (which is weak and is ignored in the model) and a contact discontinuity. The gas on the upstream side of the contact discontinuity is hotter than on the downstream side because it has passed through the strengthened bow shock.

2) The rarefaction wave propagating upstream from the energy-release front overtakes the bow shock, weakening it and restoring it to its original strength. The origin of the rarefaction wave is discussed in step 4.

3) The contact discontinuity created in step 1 convects downstream. At a point between the bow shock and the energy-release front, a new energy-release front is produced by the hotter gas on the upstream side of the contact discontinuity. The creation of a new zone of combustion, in turn, creates compression waves that propagate both upstream toward the bow shock (this is the wave that overtakes the bow shock in step 1) and downstream toward the projectile. It can be shown that the upstream and downstream compression waves are necessary to match the fluid velocity jumps across the new

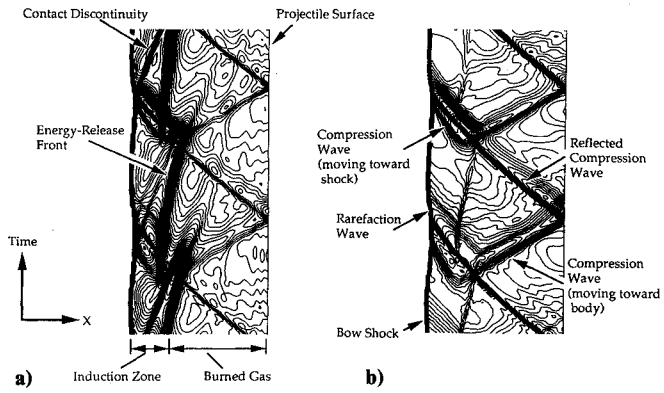

Fig. 13 Computed *x-t* diagrams of density and pressure along the stagnation streamline for the Mach 4.79 case using flux-vector splitting: a) density contours, b) pressure contours.

energy-release front and satisfy conservation of momentum (see Alpert and Toong[7]).

4) The contact discontinuity (with burning on the upstream side) eventually reaches the position of the original energy-release front. This extinguishes the original energy-release front and creates rarefaction waves that propagate in the upstream and downstream directions. The energy-release front then begins to recede toward the location of the original front as colder gas (through the bow shock of original strength) reaches the front.

From Fig. 12 it is seen that the period of an oscillation is the time required for the contact discontinuity to convect from the shock to the reaction front and then for an acoustic wave to travel back to the bow shock. If the postshock conditions are known, an analytical expression for the period of observed experimental oscillations can be found. Given a period of oscillation provided from an experiment, McVey and Toong were able to use the expression to predict the induction time for the gas mixture. Their predicted induction times agreed with previously published data. Figure 13 contains computed *x-t* diagrams of density and pressure along the stagnation streamline for the Mach 4.79 case (the flux-vector splitting algorithm was used to produce all of the computed *x-t* diagrams in this paper). A comparison of these diagrams with the McVey and Toong mechanism in Fig. 12 reveals many similarities. The density contours show a changing position of energy-release front in time that is identical to the pattern predicted by the wave interaction model (note the jagged edge of the energy-release front that appears in both Figs. 12 and 13a). In the region between the bow shock and the energy-release front, density contours also show that a contact discontinuity is created at the bow shock when a compression wave originating from the energy-release front overtakes it. The hotter gas on the upstream side of the contact discontinuity reduces the ignition delay time and causes a new energy-release front to be created. The new energy-release front is the source of the compression waves traveling in both the upstream and downstream directions. These compression waves are clearly seen in the pressure contours of Fig. 13b. The identity of the contact discontinuities labeled in Fig. 13a is verified by their absence in the pressure contours of Fig. 13b because a contact discontinuity has no pressure jump across it.

A phenomenon seen in the computations that was apparently not anticipated by McVey and Toong is the existence and/or importance of the compression waves reflecting off the projectile nose. Figure 13b shows that a compression wave created at the energy-release front travels toward the projectile nose, reflects, and eventually overtakes the bow shock. In this particular calculation, the compression wave reflects off the nose and moves toward the bow shock, overtaking it at nearly the same time that the most recently created compression wave arrives at the bow shock. The coordination between the compression wave and the reflected compression wave is not always exact, and therefore the two waves sometimes hit the bow shock at slightly different times. This tends to deform some of the structures. The importance of the reflection of the compression waves off the projectile has been recognized in the recent work of Matsuo and Fujiwara.[10]

Figure 14 contains computed *x-t* diagrams of density and pressure from a case at Mach 5.04. As in the Mach 4.79 case, the interactions between the bow shock and energy-release front correspond to the model proposed by McVey and Toong. This case is interesting because the interaction of the wave reflected off the projectile is significantly different than that seen in the Mach 4.79 case. During the time that a compression wave travels from the energy release front to the projectile body and back, two new compression waves are created (i.e., two periods have passed). The computed frequency is 820 kHz whereas the measured frequency is 1.04 MHz. A thorough discussion of this case is given in Wilson[12] along with an additional simulation of an experiment at Mach 4.18 with a much lower oscillation frequency.

Frequency Sensitivity to the Hydrogen-Air Reaction Mechanism

The nearly constant values of the instability frequency predicted by the numerical simulations using different grid sizes (375×321, 375×161, and 375×81) and two different numerical schemes suggest that the underprediction of the frequency in the computations is not caused by numerical error but by the chemical kinetic model. Wilson and MacCormack[8] established that the blunt body exothermic flowfields are quite sensitive to the following chain-branching reaction:

$$H + O_2 \rightarrow OH + O$$

In that work, flowfields were computed with two different rate expressions for this reaction. One was the original expression from the Jachimowski[11] reaction model, and the other was from Warnatz.[17] The rate expression recommended by Warnatz was adopted because it gave better agreement with experiments for the steady cases (this is the rate expression that has been used for all cases presented in this paper). To investigate the influence of the chemical kinetic mechanism on the frequency of the oscillations, the Mach 4.79 simulation is repeated using the Jachimowski rate expression. This rate expression gives shorter ignition times at high temperatures ($T > 1400$ K) than the rate constant recommended by Warnatz. This change should lead to an increase in the oscillation frequency because the induction zone is smaller and therefore the travel time between the energy-release front and the bow shock is reduced. Consistent with this expectation, the computed frequency of the oscillations increased from approximately 530 to 820 kHz. Since the experimentally determined frequency is 720 kHz, it is concluded that the uncertainties in the

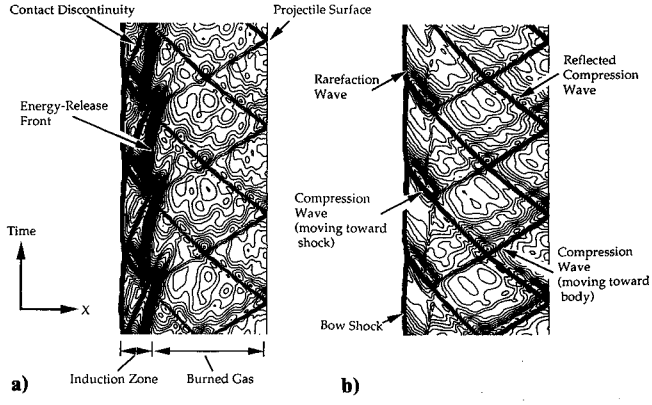

Fig. 14 Computed *x-t* diagrams of density and pressure along the stagnation streamline for the Mach 5.04 case using flux-vector splitting: a) density contours, b) pressure contours.

rate constants for the reaction mechanism could explain the differences between the experiments and the computations. The sensitivity of the oscillation frequency to the chemical reactions make the simulations a useful validation tool for kinetic models. The unsteady cases appear to provide a better measure of a kinetic model than the steady cases because the oscillation frequency can be determined with greater precision than the positions of the bow shock and energy-release front.

Finally, note that the arrival times of new compression waves and reflected pressure waves at the bow shock sometimes differ significantly (this occurred in the Mach 4.79 case with the Jachimowski rate expression[12]). The separate interactions between the bow shock and each wave lead to separate contact discontinuities and cause the x-t diagrams to appear less organized. Further investigations are required to assess the precise contribution to the combustion instability of the compression waves reflected off the projectile nose. In the present calculations they appear to have a secondary effect, but it is possible that they are more important to the instabilities seen in the large-disturbance regime investigated by Alpert and Toong.[7]

Conclusion

The successful simulations of both steady and unsteady exothermic ballistic-range experiments have added to the understanding of shock-induced combustion and have led to improvements in the numerical techniques for these types of flows; namely, proper grid resolution is a primary challenge of simulations with combustion phenomena, and these grid requirements are reduced by the use of the logarithmic transformation of the species conservation equations. The accuracy of the simulations is supported by grid refinement studies and the use of two different numerical methods, a flux-vector splitting scheme and an upwind TVD scheme. Further validation is provided by comparison to past analytical and numerical predictions of the instabilities. Finally, the simulations have reaffirmed the value of ballistic-range experiments as a source of data for high-speed flows with combustion and have demonstrated their usefulness for validating numerical methods and chemical kinetic mechanisms. It is shown that differences in the experimental and computed instability frequencies are probably due to uncertainties in the chemical reaction rates and therefore the experiments provide a means of validating proposed chemical kinetic models.

Acknowledgments

Funds for the support of this study have been allocated by the NASA Langley Research Center and by the NASA Ames Research Center under the joint research interchange number NCA2-455 and are greatly appreciated. This material is also based on work supported by a National Science Foundation Graduate Fellowship and by NASA under Hypersonic Training and Research Grant NAGW 965. The authors would also like to acknowledge the computer resources provided by the Aerothermodynamics Branch of NASA Ames, the Theoretical Flow Physics Branch of NASA Langley, and the National Aerodynamic Simulation (NAS) Program. We are most grateful to H. F. Lehr of Institute Saint Louis for providing original photographs of his ballistic-range experiments and to Leslie A. Yates for computing shadowgraph images from our flowfield solutions. We also acknowledge the support and encouragement of our advisor at Stanford University, Robert W. MacCormack.

References

[1]Ruegg, F. W., and Dorsey, W. W., "A Missile Technique for the Study of Detonation Waves," *Journal of Research of the National Bureau of Standards,* Vol. 66C, No. 1, 1962, pp. 51–58.

[2]Behrens, H., Struth, W., and Wecken, F., "Studies of Hypervelocity Firings into Mixtures of Hydrogen with Air or with Oxygen," *Tenth Symposium (International) on Combustion,* Combustion Institute, Pittsburgh, PA, 1965, pp. 245–252.

[3]Chernyi, G. G., "Onset of Oscillation in the Presence of Detonation Wave Weakening," *Journal of Applied Mathematics and Mechanics,* Vol. 33, No. 3, 1969, pp. 451–461.

[4]Lehr, H. F., Institute Saint Louis (ISL), Final Rept. 20/71, Saint-Louis, France, 1971.

[5]Lehr, H. F., "Experiments on Shock-Induced Combustion," *Astronautica Acta,* Vol. 17, Nos. 4 & 5, 1972, pp. 589–596.

[6]McVey, B. J., and Toong, T. Y., "Mechanism of Instabilities of Exothermic Hypersonic Blunt-Body Flows," *Combustion Science and Technology,* Vol. 3, No. 2, 1971, pp. 63–76.

[7]Alpert, R. L., and Toong, T. Y., "Periodicity in Exothermic Hypersonic Flows About Blunt Projectiles," *Astronautics Acta,* Vol. 17, Nos. 4 & 5, 1972, pp. 539–560.

[8]Wilson, G. J., and MacCormack, R. W., "Modeling Supersonic Combustion Using a Fully-Implicit Numerical Method," *AIAA Journal,* Vol. 30, No. 4, 1992, pp. 1008–1015; see also AIAA Paper 90-2307, July 1990.

[9]Sussman, M. A., and Wilson, G. J., "Computation of Chemically Reacting Flow Using a Logarithmic Form of the Species Conservation Equations," *Proceedings of the 4th International Symposium on Computational Fluid Dynamics* (Davis, CA), Vol. 2, Sept. 1991, pp. 1113–1118.

[10]Matsuo, A., and Fujiwara, T., "Numerical Simulation of Shock-Induced Combustion Around an Axisymmetric Blunt Body," AIAA Paper 91-1414, June 1991.

[11]Jachimowski, C. J., "An Analytical Study of the Hydrogen-Air Reaction Mechanism with Application to Scramjet Combustion," NASA TP-2791, Feb. 1988.

[12]Wilson, G. J., "Computation of Steady and Unsteady Shock-Induced Combustion over Hypervelocity Blunt Bodies," Ph.D. Thesis, Stanford Univ., Stanford, CA, Dec. 1991.

[13]MacCormack, R. W., "Current Status of Numerical Solutions of the Navier-Stokes Equations," AIAA Paper 85-0032, Jan. 1985.

[14]Candler, G. V., "The Computation of Weakly Ionized Hypersonic Flows in Thermo-Chemical Nonequilibrium," Ph.D. Thesis, Stanford Univ., Stanford, CA, June 1988.

[15]Yee, H. C., "A Class of High-Resolution Explicit and Implicit Shock-Capturing Methods," NASA TM 101088, Feb. 1989.

[16]Yates, L. A., "Images Constructed from Computed Flowfields," AIAA Paper 92-4030, July 1992.

[17]Warnatz, J., "Rate Coefficients in the C/H/O System," *Combustion Chemistry,* edited by W. C. Gardiner Jr., Springer-Verlag, New York, 1984, Chap. 5.